Simulating dimensionally reduced 4D Yang-Mills theory on a quantum computer

Nouman Butt,[*] Patrick Draper,[†] and Jiayu Shen[‡]

Illinois Quantum Information Science and Technology Center, Urbana, Illinois 61801;
Illinois Center for Advanced Studies of the Universe, Urbana, Illinois 61801; and Department of Physics,
University of Illinois at Urbana-Champaign, Urbana, Illinois 61801

We compute the low-lying spectrum of 4D SU(2) Yang-Mills in a finite volume using quantum simulations. In contrast to small-volume lattice truncations of the Hilbert space, we employ toroidal dimensional reduction to the "femtouniverse" matrix quantum mechanics model. In this limit the theory is equivalent to the quantum mechanics of three interacting particles moving inside a 3-ball with certain boundary conditions. We use the variational quantum eigensolver and quantum subspace expansion techniques to compute the string tension to glueball mass ratio near the small/large-volume transition point, finding qualitatively good agreement with large volume Euclidean lattice simulations.

I. INTRODUCTION

Quantum simulations of quantum field theories (QFTs) in the noisy intermediate-scale quantum (NISQ) era [1] will be limited by the gap between the complexity of QFTs and the available quantum resources. Currently, it is difficult to build a comparison between known Monte Carlo and quantum simulation results. In particular, gauge theories are challenging to simulate on quantum devices because of the infinite tower of states associated with each link on the lattice. To control the rapid growth in degrees of freedom requires working with small lattices and putting rather stringent truncations on the subspaces of the Hilbert space associated with bosonic degrees of freedom. Subsequently, one must take care to preserve Gauss's law and confront various limitations on what can be computed with small circuits. It is therefore interesting to explore a wide variety of approximations, truncations, encodings, and simulation techniques to make the most of available near-term systems. In the process we may hope to develop new applications and tools that will help lower the threshold for quantum supremacy in simulating high energy physics phenomena, while creating a large set of benchmark computations for calibrating quantum simulations against analytic and classical results.

In this paper we study hybrid quantum simulations of an approximation to 4D gauge theory known as the femtouniverse [2]. Complementary to the small-volume lattice approach, the approximation we use is a matrix quantum mechanics model obtained by the dimensional reduction of the 4D theory on a spatial 3-torus. The study of gauge theory on a torus was pioneered by 't Hooft [3] and the effective matrix quantum mechanics theory obtained by dimensional reduction was systematically developed by Lüscher [4], Lüscher and Münster [5], van Baal [6–8], van Baal and Koller [9,10], and others. For a comprehensive review see Ref. [11]. We focus on the SU(2) model studied in detail by van Baal and Koller [9,10]. In our quantum simulations we use the variational quantum eigensolver (VQE) [12,13] and quantum subspace expansion (QSE) [14] techniques. These are hybrid classical-quantum methods that exploit the strengths of both types of computation. With these methods we obtain the low-lying spectrum of the theory, including glueball masses and string tensions, which can be compared with the large-volume continuum limit results known from Euclidean lattice Monte Carlo [15].

The spectrum of Yang-Mills theory in infinite volume, $L^3 \to \infty$, is determined by the dynamical scale Λ where the running coupling grows strong. In small volumes $L\Lambda \ll 1$, the effective theory from integrating out Kaluza-Klein modes is accurate due to asymptotic freedom. However, it differs markedly from the large-volume limit $L\Lambda \gg 1$. At large torus volumes, the spectrum of the complete 4D theory is quite insensitive to the volume. There is a "large-small volume transition region," roughly around $\Lambda L \sim \mathcal{O}(1)$, where some strong-coupling physics of the large volume

[*]ntbutt@illinois.edu
[†]pdraper@illinois.edu
[‡]jiayus3@illinois.edu

theory is reflected with reasonable accuracy in the much simpler effective theory. This is the regime we would like to probe.

Our work is organized as follows. In Sec. II we begin by reviewing the effective Hamiltonian described in [9] and the symmetries of the effective theory, which allow the decomposition of the Hamiltonian into different super-selection sectors. In Section III we briefly review the QSE algorithm used in the calculation of excited state energies. Section IV presents our main results. We compute ground and excited state energies using classical exact diagonalization (ED), VQE + QSE simulators, and the IBM-Lima quantum computer. We discuss effects of Hilbert space truncation and different basis choices and various sources of error. We find that the string tension to glueball mass ratio of the continuum large-volume theory is reasonably well captured by VQE + QSE on the real device, working at couplings near the large/small volume transition.

The study of matrix quantum mechanics in quantum simulations is motivated both as a simpler approximation to higher-dimensional non-Abelian gauge theories, and by quantum gravity, where matrix models arise in various contexts. Interesting prior work on this subject includes [16,17]. In contrast to these works we use a minimal, gauge-invariant Hilbert space and focus on the explicit model that arises from dimensional reduction on a 3-torus, including the loop-induced effective potential and gauge field topology associated with the parent 4D theory. Dimensional reduction is also a useful approach for truncating Abelian theories while preserving some structure; previously we have studied the reduction of the Schwinger model to the quantum mechanical particle on the circle model in quantum simulation [18], where dynamics associated with an 't Hooft anomaly and the θ term [19] are transparent.

II. MATRIX MODEL FOR 4D SU(2) GAUGE THEORY

We begin by reviewing the physics of the femtouniverse. In this section, we rely heavily on the pioneering work of van Baal and Koller [9,10]. We consider pure SU(2) Yang-Mills theory in 4D on a small spatial 3-torus of length L and work in $A_0 = 0$ gauge. The Hamiltonian is

$$H = \int_{[0,L]^3} d^3\mathbf{x} \left(\frac{1}{2} g^2 E_k^a(\mathbf{x}) E_k^a(\mathbf{x}) + \frac{1}{2g^2} B_k^a(\mathbf{x}) B_k^a(\mathbf{x}) \right) \quad (1)$$

where E_k^a, B_k^a are chromoelectric and chromomagnetic fields, and g is the dimensionless strong coupling. Here k denotes the spatial index and a labels the color index. The gauge connection A_k^a is taken to satisfy periodic boundary conditions on the torus.[1]

---

[1]Working in sectors of nonzero magnetic flux would be an interesting direction for generalization.

From lattice analysis (see, e.g., [15]) we know the theory is gapped near the dynamical scale $\Lambda = \mu e^{-8\pi^2/(bg^2(\mu))}$, where μ is an arbitrary renormalization scale and $g^2(\mu)$ is the running coupling at that scale, and the spectrum becomes exponentially insensitive to L for $\Lambda L \gtrsim 1$. The effective field theory (EFT) analysis below, on the other hand, will be valid for $\Lambda L \lesssim 1$, where g may be thought of as the running coupling at the renormalization group scale $1/L$. Thus we will be particularly interested in the behavior near the small volume-large volume transition.

The proper gauge transformations of the SU(2) theory are periodic SU(2)-valued functions $g(\mathbf{x})$ acting on the connections as

$$A_k(\mathbf{x}) = g(\mathbf{x}) A_k(\mathbf{x}) g^{-1}(\mathbf{x}) - ig(\mathbf{x}) \partial_k g^{-1}(\mathbf{x}). \quad (2)$$

The classical vacuum manifold, sometimes called the "vacuum valley," is the space of flat connections modulo small gauge transformations. The vacua separate into a union of disjoint sectors characterized by different Chern-Simons numbers and related by large gauge transformations. We will work in the sector of fixed vanishing Chern-Simons number, which is acceptable as long as the states of interest have energies below the "sphaleron" energy barrier between these sectors.

We may partially fix the gauge so that the classical vacua are given by spatially constant connections that are aligned in $su(2)$ space. For convenience of illustration we can go to a gauge where the vacua are of the Abelian form

$$A_i = \frac{C_i}{L} \frac{\sigma_3}{2}. \quad (3)$$

At this point, it appears that the vacuum valley (in a fixed Chern-Simons sector) is $\mathbb{R}^3$. However, there are still residual gauge transformations, given by

$$g(\mathbf{x}) = \exp\left(-4\pi i \frac{\mathbf{x} \cdot \mathbf{n}}{L} \frac{\sigma_3}{2} \right),$$
$$g = \sigma_1. \quad (4)$$

Here n_i are integers, and $g = \sigma_1$ is the nontrivial element of the Weyl group. These gauge transformations lead to the following identifications:

$$\mathbf{C} \sim \mathbf{C} + 4\pi\mathbf{n} \quad (5)$$

$$\mathbf{C} \sim -\mathbf{C}. \quad (6)$$

Thus the vacuum valley is the orbifold $T^3/\mathbb{Z}_2$, where the torus periodicity is 4π.

At the quantum level, the continuous vacuum valley is lifted, but a discrete global symmetry is preserved. This is the $\mathbb{Z}_2$ electric center symmetry, which, in the gauge Eq. (3), acts as

$$h(\mathbf{x}) = \exp\left(-2\pi i \frac{\mathbf{x} \cdot \mathbf{n}}{L} \frac{\sigma_3}{2}\right) \qquad (7)$$

where $n_i \in \{0, 1\}$. These are not gauge transformations because $h(\mathbf{x})$ and $h(\mathbf{x} + L\mathbf{u}_i)$, where $\mathbf{u}_i$ is the ith spatial unit vector, differ by a nontrivial element of the $\mathbb{Z}_2$ center of SU(2). They are global symmetries, however, because they preserve the action and the periodic boundary conditions for the gauge field. They act on the classical vacua, which are given by $\mathbf{C} = 2\pi\mathbf{n}$, as

$$\mathbf{C} \sim \mathbf{C} + 2\pi\mathbf{n}. \qquad (8)$$

Therefore we expect 8 minima of the quantum induced potential on the vacuum valley, lying on the corners of a cube embedded in the 3-torus. We also expect that the symmetry will be unbroken and the true ground state will be similar to a symmetric linear combination of the perturbative ground states around each of these minima. In general the states can be taken to transform in representations

$$|\psi(A^h)\rangle = (-1)^{\mathbf{k} \cdot \mathbf{e}} |\psi(A)\rangle \qquad (9)$$

where $\mathbf{e}$ is $\mathbb{Z}_2$-valued electric flux labeling the representations under center [3].

It is convenient to work with an effective theory that is partway between the full theory Eq. (1) and the vacuum valley theory of the C_i alone. We split the gauge field into a linear combination of a spatially constant part and a spatially varying field:

$$A_k^a(\mathbf{x}, t) = c_k^a(t) + Q_k^a(\mathbf{x}, t). \qquad (10)$$

At small L we can integrate out Q to obtain an effective quantum mechanical theory of the c_k^a. This theory includes, in addition to the vacuum valley degrees of freedom, the "non-Abelian" or "transverse" spatially constant modes. Although it seems natural to integrate out Kaluza-Klein modes, it is not obvious that this step is consistent in a gauge theory, where the energy of a mode depends on the vacuum one is perturbing around. The validity of this step hinges on being able to stay relatively close to the origin in field space, with boundaries and suitable boundary conditions at points where the constant field effective theory breaks down. We discuss this further below.

It is also convenient to relax our identification of the vacuum valley with the σ^3 direction. By a constant gauge transformation we can "point" the vacuum valley in any direction. We will leave this gauge degree of freedom in the effective theory, then remove it later by averaging over all directions. In this formulation, the vacuum valley corresponds to c_k that are aligned in $su(2)$ space with any common direction. It may be visualized as three aligned (or antialigned) vectors in three dimensions, constrained by the

periodicities Eq. (6) to have magnitudes less than $2\pi/L$. The relative angles between the vectors then encode the transverse degrees of freedom.

The effective theory described thus far is the quantum mechanics of three interacting particles in three dimensions. In fact, we can also constrain the particles to move inside a ball,

$$r_i \equiv \sqrt{\sum_a c_i^a c_i^a} \leq \frac{\pi}{L}, \qquad (11)$$

with certain boundary conditions at π/L:

$$\left(\frac{\partial}{\partial r_i}\right)^{1-e_i} (r_i \psi(c)) \bigg|_{r_i = \frac{\pi}{L}} = 0. \qquad (12)$$

The arguments go as follows [9]. The points $r_k \in \{0, \pi\}$ in the vacuum valley are preserved by the center and Weyl transformations. This is clear in the gauge-fixed version of Eqs. (6), (8) and (11) generalizes it to the case where the vacuum valley direction is unfixed. If the wavefunction and the energy is continuous at these points, then either the wave function or its (covariant) radial derivative must vanish, depending on the electric flux quantum numbers [cf. Eq. (9)].

Continuity, however, is rather subtle. A global center transformation acts as a 2π translation on the vacuum valley, but makes a nontrivial modification to the spatial dependence of the transverse modes. Since it is a symmetry, these modes must be reordered. The transverse Kaluza-Klein modes that should be kept in a consistent effective theory are completely different from the spatially constant modes valid near the origin, once we have translated by 2π away from the origin along the vacuum valley. We should think of the points $r_k \in \{0, \pi/L\}$ as boundaries between different patches in which we have different EFTs. More precisely the "three particles in a ball" description is valid in any patch, but the map to the underlying degrees of freedom of the 4D theory changes from patch to patch. For this reason it is not immediately obvious whether wave function continuity (particularly for derivatives) must hold.

However, Ref. [9] argued that continuity properties are still expected. In brief, at weak coupling, all transverse modes are expected to be close to their ground states at $r_k = \pi/L$, and this property was reflected in the numerical analysis of [9]. At strong coupling, the transverse modes are excited. However, they also mix, and we do not expect level crossing. Continuity of the energy density then leads to the conditions Eq. (12). The interpretation of the wave function simply changes discontinuously from patch to patch.

Thus we are led to the quantum mechanics of three particles in the region Eq. (11) subject to boundary conditions Eq. (12). The effective Hamiltonian can be written as Eq. (13)

$$H_{\text{eff}} = -\frac{1}{2L}\left(\frac{1}{g^2}+\alpha_1\right)^{-1}\frac{\partial^2}{(\partial c_i^a)^2} + V_T(c) + V_l(c). \quad (13)$$

Here V_T is the "transverse" part of the effective potential which vanishes along the vacuum valley. V_l is the effective potential along the vacuum valley. These potentials take the form:

$$V_T = \frac{1}{4}\left(\frac{1}{g^2}+\alpha_2\right)F_{ij}^a F_{ij}^a + \alpha_3(F_{ij}^a F_{ij}^a)c_k^b c_k^b + \alpha_4 F_{ij}^a F_{ij}^a c_j^b c_j^b$$
$$+ \alpha_5(\det c)^2 + \cdots$$

$$V_l = \gamma_1(g)\sum_i r_i^2 + \gamma_2(g)\sum_i r_i^4 + \gamma_3(g)\sum_{i>j}r_i^2 r_j^2 + \gamma_4(g)\sum_i r_i^6$$
$$+\gamma_5\sum_{i\neq j}r_i^4 r_j^2 + \gamma_6(g)r_1^2 r_2^2 r_3^2 + \gamma_7(g)\sum_i r_i^8 + \cdots \quad (14)$$

where … indicates terms at higher orders in the fields and in the loop expansion. We only consider the Hamiltonian with $\alpha_1, \alpha_2 \neq 0$ and $\gamma_i(g) = \gamma(0)$ for $i \leq 7$ and ignore higher order terms. The effective theory is truncated at the two derivative order, so it will break down for energies above the Kaluza-Klein scale $\sim 2\pi/L$ (in addition to energies above the sphaleron energy, as discussed above.)

In order to extract the low-lying spectrum on a quantum simulator we use Hamiltonian truncation and compute the matrix elements classically. The kinetic part can be diagonalized by writing the momentum operator in spherical coordinates for "particle" i and using a spherical harmonic basis $Y_{l_i,m_i}(\theta_i,\phi_i)$ for each particle. For the radial part of momentum operator we employ two choices of basis: spherical Bessels $\chi_{n,l}^{(e)} = j_l(k_{n_i,l_i}^e r)$ with $V(r) = 0$ and a harmonic oscillator basis $\chi_{n,l}^{(e)} = r^l e^{-\omega r^2/2}M(\frac{1}{2}l+\frac{3}{4}-\epsilon_{n,l}^{(e)}/(2\omega), l+\frac{3}{2}, \omega r^2)$ with $V(r) = \frac{1}{2}\omega^2 r^2$. $M(a,b,z)$ is a confluent hypergeometric function regular at $z=0$ [9] and we have set $\omega = 1.5$. In either case the radial basis wave functions can be chosen to satisfy the Eq. (12) in each flux-sector labeled by the flux quantum number e_i. This boundary condition determines the "momenta" $k_{n,l}^e(\epsilon_{n,l}^{(e)})$ for each particle in terms of the zeros of the chosen basis functions.

In general, VQE performs better the more "physics" we can inject into the choice of basis. At strong coupling, the wave functions tend to spread out more, while for weak coupling they are more concentrated near the origin. For this reason we use the spherical Bessel basis for strong coupling $g \geq 1.2$ and the harmonic oscillator basis for weak coupling $g < 1.2$. (The spherical bessel basis exactly diagonalizes the tree-level hamiltonian at infinite coupling.) Of course, in the absence of truncation the spectrum is independent of the choice of basis, but with truncations a better choice of basis can minimize the error in eigenvalue computations.

Since we are using gauge-invariant coordinates on the vacuum valley, we can work in a fully gauge-invariant hilbert space by requiring the angular wavefunctions to be spin-singlets of SO(3). Hence the gauge invariant wave functions have no free m_i quantum numbers. (Therefore the approach here differs from other quantum simulation studies of Yang-Mills type matrix quantum mechanics models where simpler bases are used at the cost of introducing an extended Hilbert space that includes gauge-non-invariant states [17].)

In sum, the gauge-invariant Rayleigh-Ritz basis for computing the full Hamiltonian matrix are defined as follows:

$$\langle\{r_i,\theta_i,\phi_i\}_{i=1,2,3}|l_1 l_2 l_3 n_1 n_2 n_3; \mathbf{e}\rangle$$
$$= \sum_{m_1,m_2,m_3} W(l_1 l_2 l_3 m_1 m_2 m_3)\prod_{i=1}^{3}\chi_{n_i,l_i}^{e_i}(r_i)Y_{l_i m_i}(\theta_i,\phi_i)$$

$$n_i, l_i \in \mathbb{N}, \quad |l_1-l_2| \leq l_3 \leq l_1+l_2, \quad m_i \in \{-l_i, -l_i+1, ..., l_i\}$$

where $W(l_1 l_2 l_3 m_1 m_2 m_3)$ are the Wigner $3-j$ symbols.

Now we must address truncation. We use eigenvalues of the operator $\frac{\partial^2}{(\partial c_i^a)^2}$ to organize the states in Eq. (15) in an ascending order. The full Hamiltonian is infinite dimensional so we truncate it to a finite number of states. We can compute the full matrix in Eq. (13) for finite number of states by computing angular and radial matrix elements in the Rayleigh-Ritz basis. The effective hamiltonian can be further projected onto the irreducible representations of its symmetry group. For electric flux sectors $\mathbf{e} = 0$ or $\mathbf{e} = (1,1,1)$ the Hamiltonian symmetry group is the full cubic group $O(3,\mathbb{Z})$. The cubic group is a semidirect product $O(3,\mathbb{Z}) = \mathbb{Z}_2^3 \rtimes S_3$, where the $\mathbb{Z}_2$ factor corresponds to parity transformations $P_i c_k^a = -\delta_{ik}c_k^a$ and S_3 represents coordinate permutations π. These symmetries acts on the gauge-invariant states in the following manner:

$$P_i|l_1 l_2 l_3 n_1 n_2 n_3\rangle = (-1)^{l_i}|l_1 l_2 l_3 n_1 n_2 n_3\rangle$$
$$\pi|l_1 l_2 l_3 n_1 n_2 n_3\rangle = |l_{\pi(1)}l_{\pi(2)}l_{\pi(3)}n_{\pi(1)}n_{\pi(2)}n_{\pi(3)}\rangle \quad (15)$$

The cubic group has ten irreps. We focus on the parity even irreps A_1^+ (zero flux) and e_1^+ [unit flux, $\mathbf{e} = (0,0,1)$]. For $\mathbf{e} \neq 0$, $\mathbf{e} \neq (1,1,1)$ the cubic group is broken to $\mathbb{Z}_2 \rtimes (\mathbb{Z}_2^2 \rtimes S_2)$ where S_2 permutes the directions with equal electric flux. We construct the Hamiltonians classically in both sectors and numerically diagonalize them for different numbers M of states. Finally, for the case $M = 8$ we use VQE and QSE to compute the low-lying spectrum and compare with the classical exact diagonalization.

The ground state in the A_1^+ sector is used as the reference ground state for the system, identified with the true ground state in the large volume limit. The gap to the first excitation above the ground state in the A_1^+ sector is

identified as a glueball mass. The difference in ground state energies in the e_1^+ flux sector and the A_+^1 sector is identified with the energy of an electric flux string. The spectrum of the Hamiltonian in these irreps suffices to compute observables, like the square root of the string tension to the glueball mass ratio, that can be compared with values from Euclidean lattice simulations.

III. QUANTUM SUBSPACE EXPANSION FOR EXCITED STATES

As mentioned above we use VQE to obtain ground states energies. In order to obtain excited state energies, we apply the Quantum Subspace Expansion (QSE) [14] to the femtouniverse model. QSE is an extension to the VQE algorithm based on quantum measurements of a set of ansatz excitation operators in the optimal ground state estimate $|\psi(\boldsymbol{\theta}^*)\rangle$ obtained from VQE. Here $\boldsymbol{\theta} = (\theta_0, \theta_1, ..., \theta_{n_p})$ is the set of parameters in the VQE ansatz and $\boldsymbol{\theta}^*$ denotes the optimal parameters that minimize the energy.

The subspace in QSE is the Hilbert space spanned by a set of ansatz excitation operators $\{O_i\}_i$ acting on $|\psi(\boldsymbol{\theta}^*)\rangle$, i.e., a set of states $\{O_i|\psi(\boldsymbol{\theta}^*)\rangle\}_i$. To include the ground state itself, we define $O_0 = I$, the identity operator. We denote the dimension of the subspace as d^{QSE}. Then we can evaluate the Hamiltonian on the subspace as

$$H_{ij}^{\text{QSE}} \equiv \langle\psi(\boldsymbol{\theta}^*)|O_i^\dagger H O_j|\psi(\boldsymbol{\theta}^*)\rangle. \qquad (16)$$

We further require O_i to be Hermitian operators. The matrix elements of H^{QSE} can be measured on a quantum circuit, since the operator $O_i^\dagger H O_j$ can be decomposed as a linear combination of Pauli strings for the original Hilbert space. The basis $\{O_i|\psi(\boldsymbol{\theta})\rangle\}_i$ is not orthonormal, so instead of an ordinary eigenvalue problem for H^{QSE}, we will need to also compute the overlap matrix

$$S_{ij}^{\text{QSE}} \equiv \langle\psi(\boldsymbol{\theta}^*)|O_i^\dagger O_j|\psi(\boldsymbol{\theta}^*)\rangle \qquad (17)$$

and solve a generalized eigenvalue problem (GEVP)

$$H^{\text{QSE}}\mathbf{v} = \lambda S^{\text{QSE}}\mathbf{v}. \qquad (18)$$

The eigenvector $\mathbf{v}$ found this way does not directly give the eigenwavefunctions but needs a further transformation explained in Appendix B. For our purpose, we do not use this transformation and only focus on the energies given by λ. Similar to H^{QSE}, the matrix elements of S^{QSE} can also be measured on the quantum circuit. When the ansatz excitation operators are chosen effectively, solving the GEVP yields a set of eigenstates and eigenenergies that are close to the lowest d^{QSE} eigenstates and eigenenergies of H in the original Hilbert space.

In the example of 3 qubits with the truncation $M = 2^3 = 8$, we choose O_i as $O_0 = III$, $O_1 = XII$, $O_2 = IXI$, $O_3 = IIX$ in the Pauli-string notation. This set of ansatz operators becomes approximately accurate when using the spherical Bessel function basis in the large-g limit, since the lowest excitations are approximately the single-qubit-flipped states from the ground state.

Measuring the matrix elements of H^{QSE} and S^{QSE} requires evaluations of Pauli strings expectation values at the state $|\psi(\boldsymbol{\theta}^*)\rangle$. Since the total number of Pauli strings in the 3-qubit case is only 64 and our Hamiltonian is relatively dense, we measure all the 64 Pauli strings. It is worth noting that the quantum computational resource required at QSE in our case is significantly lower than VQE, because the VQE does quantum measurements at multiple positions in the space of $\boldsymbol{\theta}$, but in QSE, $\boldsymbol{\theta}$ is fixed to $\boldsymbol{\theta}^*$.

The ground state energy obtained from QSE is not necessarily the same as the ground state energy from the prior VQE. We include the results for ground state energy from VQE, and the first excited state energies from the follow-up QSE.

IV. RESULTS FROM NUMERICAL SIMULATION AND REAL QUANTUM HARDWARE

We implement our numerical simulation on the measurement-based Aer simulator in Qiskit [20], a python framework for quantum computation. We work in units where the volume is $L = 1$ and we scan over the running coupling $g(L)$, which is equivalent to adjusting the dimensionless combination ΛL.

We also implement the VQE and QSE computation on the IBM quantum computer Lima. In these computations we use the $M = 8$ truncation with 3 qubits and test three values of the coupling, $g \in \{1.8, 2.2, 2.6\}$. We use measurement error mitigation [21] to reduce the effect of noise on the real quantum hardware.

The effective Hamiltonian does not exhibit the canonical form of spin or fermionic Hamiltonian. The simplest digital quantum encoding scheme involves expanding the Hamiltonian in a Pauli string (tensor product of Paulis) basis. This naive encoding, for a generic Hamiltonian, leads to number of Pauli strings that is exponential in the number of qubits rather than polynomial.[2]

We begin by performing multiple runs of VQE without quantum noise with $N_{\text{shots}} = 10,000$ for a given coupling, starting from a fully random initial point for every run. This

---

[2]This is a fairly generic issue when the Hamiltonian of a model with gauge invariance is constructed on a gauge invariant Hilbert space. Parts of the Hamiltonian (for example, acting on a single plaquette [22]) are typically dense in the Pauli string basis irrespective of the truncation. In such cases the scaling can be improved by a square root [23] by Pauli grouping, by a more refined choice of encoding, or by applying approximation methods to reduce the density. For low qubit numbers we simply work with the naive encoding.
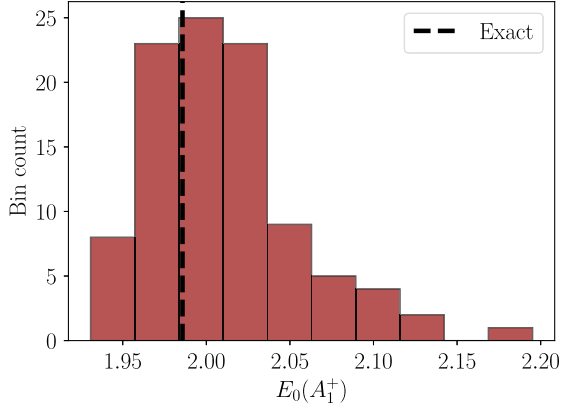
FIG. 1. Histogram of 100 VQE runs vs classical exact diagonalization result at $g = 2.6$ for A_1^+ irrep on Aer simulator with $N_{\rm shots} = 10{,}000$.
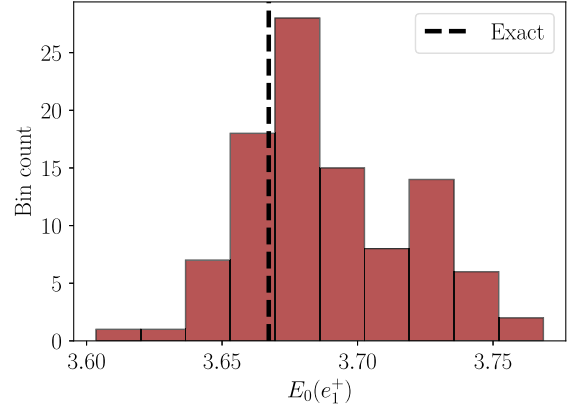

FIG. 2. Histogram of 100 VQE runs vs classical exact diagonalization result at $g = 2.6$ for e_1^+ irrep on Aer simulator with $N_{\rm shots} = 10{,}000$.

is a test of whether the ansatz is able to reliably find the correct result. In Figs. 1 and 2 we show histograms of A_1^+ and e_1^+ values obtained from 100 VQE runs with $g = 2.6$. The results are clustered around the exact diagonalization value to within a few percent. The fact that VQE can occasionally return results below the truth value is a consequence of shot noise and the Pauli string decomposition; in our simulations we use 10000 shots, so few-% errors of this type are expected.[3]

The fidelity between the initial ansatz state and the true ground state, the flatness of energy landscape around local minima [24], and limitations arising from the classical optimizer are the dominant factors which affect the shape of these distributions. In particular the flatness of energy landscape around a local minima can lead to a VQE result which is far away from the rest of the values, even in simulation without quantum noise.

In Figs. 3 and 4 we show the VQE simulation results (without quantum noise) for a range of g values and compare to the ED values. We also show IBM-Lima results in Figs. 3 and 4 with $M = 8$ states(3-qubits) for $g = 1.8$, 2.2, 2.6. We used the measurement error mitigation [21] to reduce the effect of noise on the real quantum hardware.
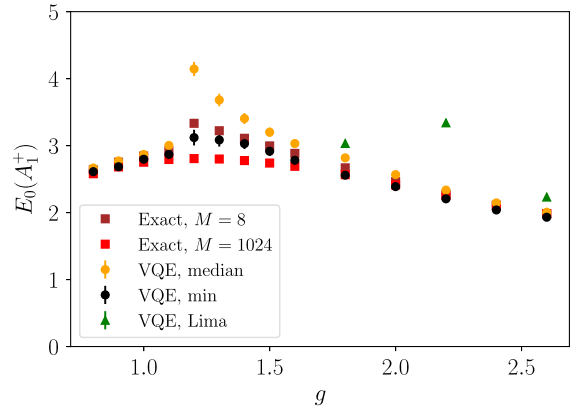

FIG. 3. VQE versus classical exact diagonalization result for A_1^+ irrep.

We present both the VQE minimum and median[4] over 100 runs to emphasize the impact of performing multiple runs.

For most values of g, we observe excellent agreement for the ground state results obtained with high-truncation ED (1024 states), low truncation ED (8 states), and the VQE simulations (without quantum noise but only shot noise) with both the minimum and the median taken over runs. However, a clear discontinuity is apparent at $g = 1.2$, and for $1.2 \lesssim g \lesssim 1.5$, the spread in results is pronounced. This discontinuity arises from the change in basis employed as we go from the weak to the strong coupling regime. The discontinuity is invisible for $M = 1024$, indicating that with a large truncation cutoff the results are essentially basis-independent, but the $M = 8$ truncation shows a

---

[3]This is not a violation of the variational principle. The expectation value of the Hamiltonian is estimated from a sum of expectation values of Pauli strings appearing in the decomposition of H, and these individual terms accrue uncorrelated statistical errors from the finiteness of $N_{\rm shots}$. It can happen that, say, a term in the Pauli decomposition of H that lowers the ground state energy experiences a downward statistical fluctuation in the shots-based estimate of its expectation value in a given state. If the state is very close to the true ground state, this can lead to an expectation value estimate for H that is below the true ground state energy. It is purely a $1/\sqrt{(N_{\rm shots})}$ effect and disappears in the limit that expectation values are measured exactly, which is the limit where the variational principle applies. In Appendix C we elaborate on this phenomenon in a toy model.

[4]We order the energies first. When $n_{\rm runs}$ of VQE is even, the $(n_{\rm runs}/2)$th run (slightly skewed toward the lower side) is chosen as the median, so that the median is always a single sample, not an average of 2 samples. When $n_{\rm runs}$ of VQE is odd, the usual median is taken.
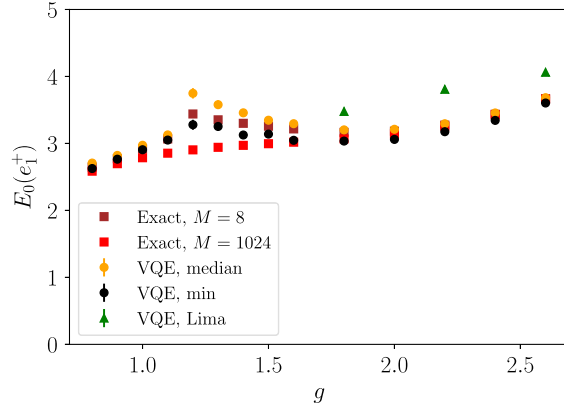
FIG. 4.   VQE versus classical exact diagonalization result for e_1^+ irrep.

FIG. 5.   QSE versus classical exact diagonalization result for A_1^+ irrep excited state.

FIG. 6.   Lightest glueball mass in the A_1^+ sector.

discontinuity. In this case we also see that taking the minimum over VQE runs generally gets closer to the exact value than the VQE median. The disagreement between median and minimum is a consequence of significant numbers of runs in which the VQE algorithm became stuck in spurious local minima, unable to escape due to the flatness of the energy landscape around the local minima. In such cases the minimum is the most reasonable estimate of the ground state energy. However, the minimum can undershoot the exact result due to shot noise, so in some circumstances the median may be preferable. (See Footnote 3 and Appendix C for further discussion of this point.)

The IBM-Lima results for $g = 1.8, 2.2, 2.6$ are generally around $\sim 20\%$ above the simulations without quantum noise and exact results, apart from the result in the A_1^+ sector for $g = 2.2$ which is significantly higher. The $g = 2.2$ experiment was performed on the same quantum computer but on a different day from the $g = 1.8$ and $g = 2.6$ experiments. The larger discrepancy from simulations without quantum noise exhibited by the $g = 2.2$ experiment may reflect a day-to-day variation in the quality of the quantum computer in the lab and calibration of the apparatus therein.

Figure 5 shows the first excited state energy in the A_1^+ sector, comparing the QSE + VQE result to exact diagonalization. Figure 6 shows the glueball mass m_{0^+}, which is the gap between this state and the ground state $m_{0^+} = E_1(A_1^+) - E_0(A_1^+)$. The effect of the truncation to $M = 8$ states substantially overestimates the glueball mass for $g \lesssim 2$, relative to the $M = 1024$ truncation. This is seen already in exact diagonalization and the situation improves for larger values of g. We repeat the same procedure of multiple runs, using optimal parameters from VQE runs, including IBM-Lima runs for $g = 1.8, 2.2, 2.6$. The QSE results from the minimum run of VQE typically show better performance than the QSE result from the median run of VQE. For this reason we show only the minimum results in Fig. 6. These results converge well to the low-truncation exact diagonalization values at both large $g \gtrsim 1.8$ and small
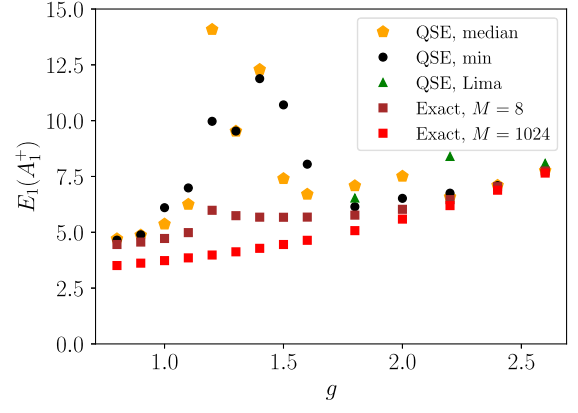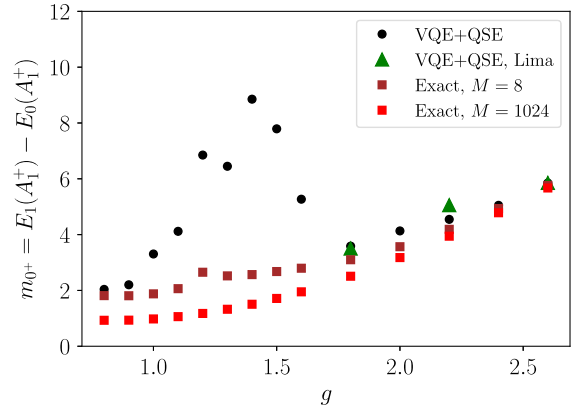
$g \lesssim 1$, and to the high-truncation values at large g. In addition, the m_{0^+} results on real hardware agree well with the exact results, even in the worst case at $g = 2.2$ ($\sim 30\%$), where the upward bias partially cancels in the energy difference.

In Fig. 7 we show the string tension σ given by the energy gap between the ground states of the e_1^+ and A_1^+ sectors, $\sigma L = E_0(e_1^+) - E_0(A_1^+)$ (where computationally we work in units with $L = 1$.) The tension is highly suppressed for small couplings, reflecting the exponential cost of tunneling through the quantum-induced barriers separating center-conjugate vacua. The suppression disappears at larger couplings as wave functions are more readily able to penetrate the barrier, signalling the onset of large volume physics.

We emphasize that the largest values of g we consider coincide with the breakdown of the dimensionally reduced effective quantum mechanics as a good description of the low-lying states of the full 4D theory. Two neglected physical effects come into play around the same time: Kaluza-Klein masses become comparable to the lightest glueball mass and string tension, as does the sphaleron
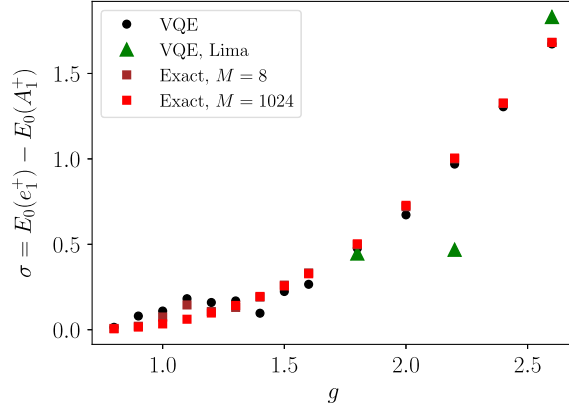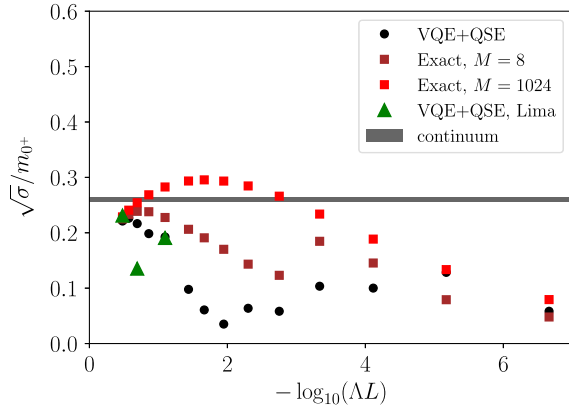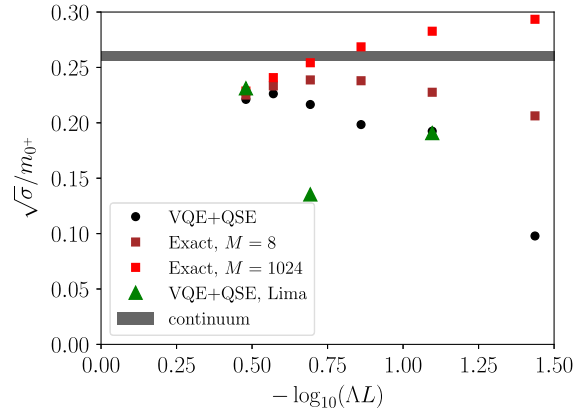
FIG. 7. String tension, $g \in [0.8, 2.6]$.

FIG. 8. Square root of string tension to glueball mass ratio versus $-\log_{10}(\Lambda L)$.

FIG. 9. Square root of string tension to glueball mass ratio.

energy barrier separating sectors of varying Chern-Simons number [11]. These are large-volume effects that cannot be captured by the matrix model effective theory.

Nonetheless, as we approach $\Lambda L \sim 1$ from above, some of the large-volume physics is quantitatively captured by

the matrix model. In Fig. 8 we plot the square root of the string tension-to-glueball mass ratio $\sqrt{\sigma}/m_{0^+}$ against $-\log_{10}(\Lambda L)$, using the 2-loop $\overline{\text{MS}}$ estimate for Λ,

$$\Lambda L = e^{-\frac{1}{2\beta_0 g^2}}(\beta_0 g^2)^{\frac{-\beta_1}{2\beta_0^2}}, \quad \text{where} \quad \beta_0 = \frac{N}{16\pi^2}\frac{11}{3} \quad \text{and} \quad \beta_1 = \left(\frac{N}{16\pi^2}\right)^2\frac{34}{3}$$

with $N = 2$. We have also added the continuum, large-volume extrapolation from lattice results [15] as a solid horizontal line. We see that the simulations converge to within about 15% of the continuum, large-volume value for this observable in the largest volumes (left-hand side of the plot), and agreement is found using IBM-Lima for the largest value of g. In Fig. 9 we zoom in on the large g region of this plot.

V. CONCLUSIONS AND OUTLOOK

In the near-term, quantum simulations of the type performed here will be limited by noise. We find, for example, that IBM Lima does not give stable results with 4 qubits for our Hamiltonian. This is mainly because of the increased circuit depth and thus the accumulated error from noise. However, there are several directions for improvement that could help push the reach of VQE simulations future, including device-specific choices of gates, optimizing the complexity of the ansatz, quantum error correction [25], and theoretical improvements in the algorithms, such as utilizing commuting families of Pauli strings [26] to reduce the number of measurements. Recent developments of Koopman operator learning techniques for quantum optimization [27] can accelerate VQE when using gradient-based optimizers, saving quantum resources for other use.

Compared to the lattice approaches, the femtouniverse, as an example of effective theory of the low-momentum modes, represents a different step toward ultimate target of quantum simulations for high energy physics. Using a relatively small number of qubits on a quantum computer, we can already simulate some 4D physics and obtain qualitatively reasonable results in agreement with 4D lattice simulations on classical computers. The dimensional reduction approach supplies a different type of regulator from the lattice regulator, and is relevant to other models of interest in high energy physics including models of quantum gravity [28]. The manifest gauge invariance in the quantum basis also helps reduce the number of dimension of the Hilbert space and thus the number of qubits.

In this paper, using VQE and QSE, we find that the currently available noisy quantum computers can already produce the glueball mass and string tension for the 4D SU (2) Yang-Mills theory qualitatively in agreement with other approaches. Our approach only requires a very small number of qubits, but the Hamiltonian matrix has a relatively large number of elements, and thus may require a relatively deep quantum circuit and big number of Pauli strings. The encoding of the basis states into the qubit computational basis is not fine tuned, and Hamiltonian matrix elements are all kept without specific ordering or

approximation. In addition, with more delicate choice of the representation of the femtouniverse on the quantum computer, it will be interesting to study if the depth of the ansatz can be reduced without loss of essential physics.

The SU(2) Yang-Mills matrix quantum mechanics model studied here can be extended in a few different directions. Adding higher-momentum modes and their interaction with the zero-momentum modes can improve the approximation to the complete 4D Yang-Mills theory, while adding fermions can connect to more physical models of interest. Future study on how the complexity and performance scales with N for the SU(N) Yang-Mills theory will likewise inform the scalability and generalizability of the approach.

ACKNOWLEDGMENTS

APPENDIX A: ED RESULTS

Table I contains exact diagonalization results for ground state energies of the irreps A_1^+, e_1^+ and the first excited energy for A_1^+ denoted by $(A_1^+)'$.

APPENDIX B: DETAILS OF VQE AND QSE

The ansatz wave function for the ground state of the Hamiltonian H can be constructed on a quantum circuit as $|\psi(\boldsymbol{\theta})\rangle = U(\boldsymbol{\theta})|0\rangle$, where $U(\boldsymbol{\theta})$ is a unitary operator consisting of quantum gates parametrized by $\boldsymbol{\theta} = (\theta_0, \theta_1, \ldots, \theta_{n_p})$, and $|0\rangle$ is the default starting state on the quantum circuit. The target energy function to be minimized is

$$E(\boldsymbol{\theta}) \equiv \langle \psi(\boldsymbol{\theta})|H|\psi(\boldsymbol{\theta})\rangle. \tag{B1}$$

$\boldsymbol{\theta}^* \equiv \mathrm{argmin}_{\boldsymbol{\theta}} E(\boldsymbol{\theta})$ gives an approximate ground state of H, and the energy evaluated at $\boldsymbol{\theta}^*$ gives the approximate ground state energy. The Hamiltonian is encoded into the quantum circuit by a linear decomposition in terms of Pauli strings. We also refer to the review [13] for more details of VQE.

In VQE computations we use the RealAmplitudes ansatz with linear entanglement and reps = 2. There are 9 parameters in the ansatz. RealAmplitudes only gives a real-valued wave function, and the eigenstates of the Hamiltonian we consider can always be constrained to be real-valued, so this choice of ansatz is reasonable for our task with a relatively small number of parameters. We use the optimizer COBYLA [29] with maxiter = 1000 (maximum number of iterations), rhobeg = 0.5 (reasonable initial changes to the variables), tol = 0.001 (final accuracy in the optimization). The number of shots for quantum measurement is 10,000 so that the statistical error associated with measurement is small. We also use the measurement error mitigation with 10,000 shots when constructing the calibration matrix.

TABLE I. Ground state and the first excited state energies of the irrep A_1^+, and the ground state energies of the irrep e_1^+ from exact diagonalization with truncations $M = 1024, 16, 8$. As described in the text, we change the basis used for the truncation at $g = 1.2$.

	A_1^+			$(A_1^+)'$			e_1^+		
g	1024	16	8	1024	16	8	1024	16	8
0.8	2.580	2.617	2.638	3.540	4.183	4.452	2.585	2.633	2.645
0.9	2.682	2.732	2.752	3.651	4.303	4.562	2.697	2.758	2.772
1.0	2.752	2.821	2.844	3.763	4.486	4.722	2.786	2.865	2.919
1.1	2.792	2.885	2.921	3.878	4.735	4.985	2.854	2.962	3.066
1.2	2.806	2.966	3.332	3.999	4.986	5.984	2.903	3.151	3.439
1.3	2.799	2.923	3.222	4.134	4.844	5.743	2.941	3.107	3.352
1.4	2.776	2.868	3.109	4.285	4.792	5.676	2.971	3.078	3.300
1.5	2.739	2.803	2.995	4.454	4.804	5.672	2.995	3.062	3.256
1.6	2.690	2.731	2.883	4.641	4.872	5.679	3.018	3.058	3.216
1.8	2.565	2.578	2.668	5.074	5.164	5.768	3.068	3.081	3.165
2.0	2.412	2.417	2.462	5.590	5.622	6.028	3.141	3.145	3.182
2.2	2.251	2.253	2.273	6.194	6.206	6.463	3.256	3.258	3.273
2.4	2.101	2.102	2.110	6.884	6.889	7.045	3.428	3.429	3.435
2.6	1.980	1.981	1.985	7.652	7.654	7.746	3.663	3.664	3.667

When implementing QSE, we make measurements of all $4^3 = 64$ Pauli strings for the 3-qubit system, based on the same ansatz as VQE at θ^*. We again use 10,000 shots for each Pauli string evaluation and also the measurement error mitigation.

We denote the nonorthogonal basis by $\{|\phi_i\rangle\}$ ($i = 0, 1, \ldots, d^{\text{QSE}} - 1$ where $d^{\text{QSE}} = 4$ in our case).

The transformation between $\{|\phi_i\rangle\}$ and an orthonormal basis $\{|\psi_i\rangle\}$ is

$$|\psi_i\rangle = P^*_{ij}|\phi_j\rangle. \tag{B2}$$

Then the following operator identity holds

$$PSP^\dagger = I, \tag{B3}$$

where

$$S_{ij} = \langle\phi_i\rangle\phi_j \tag{B4}$$

is the overlap matrix. In the QSE basis, $S = S^{\text{QSE}}$ in the main text. An operator O when acting on the nonorthonormal basis transforms as

$$O' = SP^\dagger OPS. \tag{B5}$$

With the Hamiltonian matrix in the nonorthogonal basis

$$H^{\text{QSE}}_{ij} = \langle\phi_i|H|\phi_j\rangle \tag{B6}$$

we need to solve the GEVP

$$H^{\text{QSE}}\mathbf{v} = \lambda S\mathbf{v}. \tag{B7}$$

We can transform the eigenvector $\mathbf{v}$ back by

$$\mathbf{u} = PS\mathbf{v}, \tag{B8}$$

where $\mathbf{u}$ is the wave function of the eigenstate in the original orthonormal basis $\{|\psi_i\rangle\}$.

APPENDIX C: TOY MODEL OF VQE UNDERSHOOT

As described in the main text and footnote 3, measuring expectation values of the Hamiltonian with a Pauli string decomposition and a finite number of shots can occasionally lead to VQE estimates for the ground state energy below the true value. This occurs when the state is actually quite close to the true ground state and downward fluctuations affect particular terms in the string expansion of the Hamiltonian.

Since this phenomenon may be unfamiliar and somewhat counter to variational principle intuition, we illustrate it with a simple example. Consider the one-qubit Hamiltonian

$H = \frac{1}{\sqrt{2}}(\sigma_x + \sigma_z)$. In the computational basis the true ground state $|\psi_g\rangle$ is a certain linear combination $a|0\rangle + b|1\rangle$ with energy $E_g = -1$. Suppose we are given the exact ground state and we wish to measure the energy with a finite number of shots. In the Pauli string decomposition approach, we first measure $\langle\psi_g|\sigma_x|\psi_g\rangle$ and then $\langle\psi_g|\sigma_z|\psi_g\rangle$. Even on a perfect quantum device, these two measurements will experience uncorrelated shot noise. Suppose, for an extreme example, that we estimate the two expectation values with a single shot each. One of the four possible outcomes is $(-1, -1)$, and the resulting estimate for the ground state energy is $-\sqrt{2}$, below the true value.

This "strong violation of the variational principle" only occurred because we performed an extremely poor statistical estimate of the expectation values. Increasing N_{shots}, the estimates improve and the likelihood of a strong downward fluctuation decreases. Small downward fluctuations, on the order of $1/\sqrt{N_{\text{shots}}}$, are still possible, however. In Fig. 10 we show the distribution of expectation values of H obtained from shots-based measurements of $\langle\psi_g|\sigma_x|\psi_g\rangle$ and $\langle\psi_g|\sigma_z|\psi_g\rangle$ given the exact ground state $|\psi_g\rangle$. We perform 10^5 trials with 10^3 shots in the measurement of each expectation value. The results are consistent with a Gaussian centered on the true ground state energy with variance $1/\sqrt{2N_{\text{shots}}}$.

In a real VQE experiment, the ground state is never determined exactly. However, if the state obtained is sufficiently close to the true ground state, such that the true expectation value of the Hamiltonian in the state matches the true ground state energy to within a fraction of order $\mathcal{O}(1/\sqrt{N_{\text{shots}}})$, downward fluctuations of this type can carry the shots-based expectation value estimate below
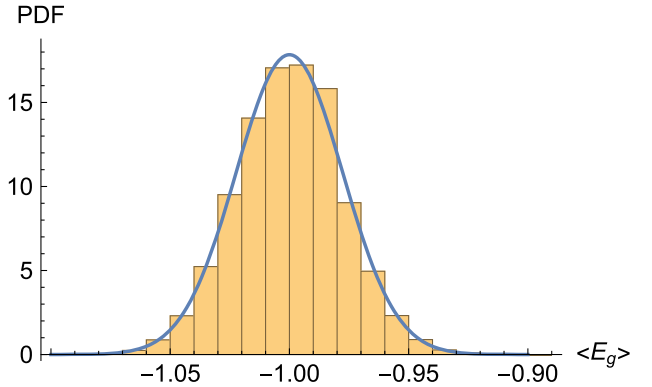

FIG. 10. Probability density function (PDF) of expectation values of $H = \frac{1}{\sqrt{2}}(\sigma_x + \sigma_z)$, in the true ground state obtained from separate shots-based measurements of σ_x and σ_z. 10^3 shots are used in each separate measurement and the PDF is obtained from 10^5 trials. Shot noise, which is uncorrelated between the two operator measurements, can produce an estimated ground state energy below the true value by an amount of order $1/\sqrt{2N_{\text{shots}}}$. The solid curve shows a Gaussian centered on the true ground state energy, -1, with variance $1/\sqrt{2N_{\text{shots}}}$.

the true ground state energy. We observe this phenomenon occasionally in our analysis (cf., Figs. 1 and 2.)

APPENDIX D: COMPARISON BETWEEN GROUND STATE ENERGIES FROM VQE AND QSE

We compare the ground state energy distributions obtained from VQE and QSE in Fig. 11 which are the same set of runs used for the figures in the main text. The QSE runs are based on the states found by pure VQE runs presented in the same figure. The distributions of VQE and QSE generally overlap with each other within the distributions' standard deviation, which shows an internal consistency. We in principle can choose either the VQE or QSE ground state energies, but empirically, as is illustrated in Fig. 11, the VQE ground state energies are closer than the exact values and thus are better to use. The QSE ground state energies are obtained from solving the GEVP instead of directly solving a optimization problem, whereas VQE is an optimization procedure, so it is not common for the ground state energy from the QSE to be even lower than the VQE ground state energy. In the VQE distributions we also see the shot-noise effect described in Appendix C.
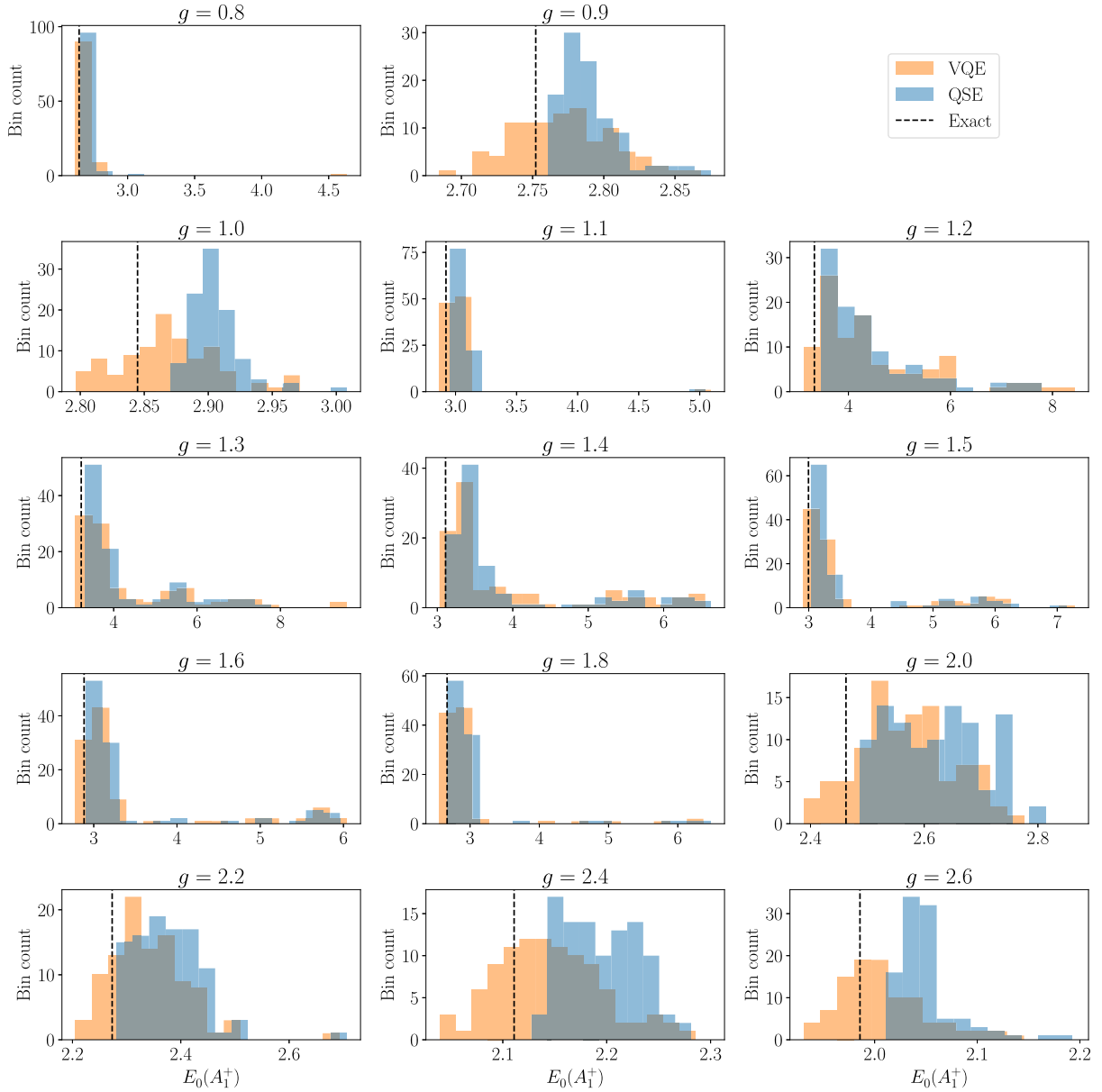

FIG. 11. Comparison of the ground state energies of the A_1^+ irrep between VQE and QSE. 100 runs are performed for each value of g. The QSE is based on the ground state found by VQE for each run. The two histograms for every g overlap generally within the standard deviation of the two distributions.

[1] John Preskill, Quantum computing in the NISQ era and beyond, Quantum **2,** 79 (2018).

[2] J. D. Bjorken, Elements of quantum chromodynamics, Prog. Math. Phys. **4,** 423 (1979).

[3] Gerard 't Hooft, A property of electric and magnetic flux in nonabelian gauge theories, Nucl. Phys. **B153,** 141 (1979).

[4] M. Luscher, Some analytic results concerning the mass spectrum of Yang-Mills gauge theories on a torus, Nucl. Phys. **B219,** 233 (1983).

[5] M. Lüscher and G. Münster, Weak-coupling expansion of the low-lying energy values in the SU(2) gauge theory on a torus, Nucl. Phys. **B232,** 445 (1984).

[6] Pierre van Baal, On the ratio of the string tension and the glueball mass squared in the continuum, Nucl. Phys. **B264,** 548 (1986).

[7] Pierre Van Baal, Gauge theory in a finite volume, Acta Phys. Pol. B **20,** 295 (1989).

[8] Pierre van Baal, *Beyond the Gribov Horizon in the Femto Universe* (Springer US, Boston, MA, 1990), pp. 131–152.

[9] Jeffrey Koller and Pierre van Baal, A non-perturbative analysis in finite volume gauge theory, Nucl. Phys. **B302,** 1 (1988).

[10] Pierre van Baal and Jeffrey Koller, QCD on a torus, and electric flux energies from tunneling, Ann. Phys. (N.Y.) **174,** 299 (1987).

[11] Pierre Van Baal, QCD in a finite volume, in *At The Frontier of Particle Physics: Handbook of QCD (In 3 Volumes)* (World Scientific, Singapore, 2001), pp. 683–760.

[12] Alberto Peruzzo, Jarrod McClean, Peter Shadbolt, Man-Hong Yung, Xiao-Qi Zhou, Peter J. Love, Alán Aspuru-Guzik, and Jeremy L. O'brien, A variational eigenvalue solver on a photonic quantum processor, Nat. Commun. **5,** 1 (2014).

[13] Jules Tilly, Hongxiang Chen, Shuxiang Cao, Dario Picozzi, Kanav Setia, Ying Li, Edward Grant, Leonard Wossnig, Ivan Rungger, George H. Booth *et al.*, The variational quantum eigensolver: A review of methods and best practices, Phys. Rep. **986,** 1 (2022).

[14] Jarrod R. McClean, Mollie E. Kimchi-Schwartz, Jonathan Carter, and Wibe A. de Jong, Hybrid quantum-classical hierarchy for mitigation of decoherence and determination of excited states, Phys. Rev. A **95,** 042308 (2017).

[15] Michael J. Teper, Glueball masses and other physical properties of SU(N) gauge theories in $D = (3 + 1)$: A review of lattice results for theorists, arXiv:hep-th/9812187.

[16] Hrant Gharibyan, Masanori Hanada, Masazumi Honda, and Junyu Liu, Toward simulating superstring/m-theory on a quantum computer, J. High Energy Phys. 07 (2021) 140.

[17] Enrico Rinaldi, Xizhi Han, Mohammad Hassan, Yuan Feng, Franco Nori, Michael McGuigan, and Masanori Hanada, Matrix-model simulations using quantum computing, deep learning, and lattice Monte Carlo, PRX Quantum **3,** 010324 (2022).

[18] Jiayu Shen, Di Luo, Chenxi Huang, Bryan K. Clark, Aida X. El-Khadra, Bryce Gadway, and Patrick Draper, Simulating quantum mechanics with a θ-term and an 't Hooft anomaly on a synthetic dimension, Phys. Rev. D **105,** 074505 (2022).

[19] G.'t Hooft, *Naturalness, Chiral Symmetry, and Spontaneous Chiral Symmetry Breaking* (Springer US, Boston, MA, 1980), pp. 135–157.

[20] M. D. Sajid Anis, Abby-Mitchell, Héctor Abrahamand *et al.*, Qiskit: An open-source framework for quantum computing, https://dx.doi.org/10.5281/zenodo.2562110.

[21] George S. Barron and Christopher J. Wood, Measurement error mitigation for variational quantum algorithms, arXiv:2010.08520.

[22] Anthony Ciavarella, Natalie Klco, and Martin J. Savage, Trailhead for quantum simulation of SU(3) Yang-Mills lattice gauge theory in the local multiplet basis, Phys. Rev. D **103,** 094501 (2021).

[23] Ben Reggio, Nouman Butt, Andrew Lytle, and Patrick Draper, Fast partitioning of Pauli strings into commuting families for optimal expectation value measurements of dense operators, arXiv:2305.11847.

[24] Jarrod R McClean, Sergio Boixo, Vadim N. Smelyanskiy, Ryan Babbush, and Hartmut Neven, Barren plateaus in quantum neural network training landscapes, Nat. Commun. **9,** 1 (2018).

[25] Asher Peres, Reversible logic and quantum computers, Phys. Rev. A **32,** 3266 (1985).

[26] Pranav Gokhale *et al.*, Minimizing state preparations in variational quantum eigensolver by partitioning into commuting families, arXiv:1907.13623.

[27] Di Luo, Jiayu Shen, Rumen Dangovski, and Marin Soljačić, Koopman operator learning for accelerating quantum optimization and machine learning, arXiv:2211.01365.

[28] T. Banks, W. Fischler, S. H. Shenker, and L. Susskind, *m* theory as a matrix model: A conjecture, Phys. Rev. D **55,** 5112 (1997).

[29] Michael J. D. Powell, A direct search optimization method that models the objective and constraint functions by linear interpolation, in *Advances in Optimization and Numerical Analysis* (Springer, New York, 1994), pp. 51–67.